Cycling Behavior of NCM523/Graphite Lithium-Ion Cells in the 3–4.4 V Range: Diagnostic Studies of Full Cells and Harvested Electrodes

James A. Gilbert,[a] Javier Bareño,[a] Timothy Spila,[b] Stephen E. Trask,[a] Dean J. Miller,[a] Bryant J. Polzin,[a] Andrew N. Jansen,[a,*] and Daniel P. Abraham[a,*,z]

[a]*Argonne National Laboratory, Argonne, Illinois 60439, USA*
[b]*University of Illinois at Urbana-Champaign, Urbana, Illinois 61801, USA*

Energy density of full cells containing layered-oxide positive electrodes can be increased by raising the upper cutoff voltage above the present 4.2 V limit. In this article we examine aging behavior of cells, containing $LiNi_{0.5}Co_{0.2}Mn_{0.3}O_2$ (NCM523)-based positive and graphite-based negative electrodes, which underwent up to ∼400 cycles in the 3–4.4 V range. Electrochemistry results from electrodes harvested from the cycled cells were obtained to identify causes of cell performance loss; these results were complemented with data from X-ray photoelectron spectroscopy (XPS) and secondary ion mass spectroscopy (SIMS) measurements. Our experiments indicate that the full cell capacity fade increases linearly with cycle number and results from irreversible lithium loss in the negative electrode solid electrolyte interphase (SEI) layer. The accompanying electrode potential shift reduces utilization of active material in both electrodes and causes the positive electrode to cycle at higher states-of-charge. Full cell impedance rise on aging arises primarily at the positive electrode and results mainly from changes at the electrode-electrolyte interface; the small growth in negative electrode impedance reflects changes in the SEI layer. Our results indicate that cell performance loss could be mitigated by modifying the electrode-electrolyte interfaces through use of appropriate electrode coatings and/or electrolyte additives.

The pursuit of high energy density lithium-ion batteries for transportation applications continues in order to increase the driving range of vehicles on a single charge. Because graphite (Gr) remains the active material of choice in the negative electrode, the search mainly revolves around layered oxides for the positive electrode. In recent years there has been immense interest in the lithium and manganese-rich layered oxides which are capable of delivering high energy density cells.[1–10] This interest has ebbed somewhat because the voltage fade exhibited by these oxides lowers the usable energy, and complicates state-of-charge determination, of the battery cells.[11–19] As research continues to combat voltage fade, interest in the lithium-stoichiometric, manganese-bearing, nickel-rich layered oxides ($Li_{1+x}Ni_aCo_bMn_cO_2$, x typically <0.05) has been rekindled.[20–26] Oxides, such as $LiNi_{0.5}Co_{0.2}Mn_{0.3}O_2$ (NCM523), $LiNi_{0.6}Co_{0.2}Mn_{0.2}O_2$ (NCM622), and $LiNi_{0.8}Co_{0.1}Mn_{0.1}O_2$ (NCM811), are among the many candidates being studied as part of the Department of Energy's Applied Battery Research (ABR) for Transportation program. These materials exhibit oxide-specific charge- and energy-densities exceeding 200 Ah/kg and 700 Wh/kg when cycled between 3–4.5 V vs. Li/Li$^+$ at low rates.

In this article we focus our attention on the NCM523 oxide which has been the subject of several recent articles. For example, Bak et al. conducted in situ X-ray diffraction studies on various (delithiated) $Li_xNi_aCo_bMn_cO_2$ materials and concluded that NCM523 is an optimized composition offering the thermal stability of lower-Ni oxides (such as NCM333) while displaying capacities closer to the higher-Ni oxides (such as NCM811).[27] From AC impedance and DC polarization studies Amin and Chiang reported that the electronic conductivity of NCM523 increases with decreasing Li-content, from 10^{-7} S/cm for a fully-lithiated oxide ($Li_{1.0}$) to 10^{-2} S/cm for a significantly delithiated ($Li_{0.25}$) oxide.[28] Dixit et al. confirmed from first

principle-based simulation studies that during oxide delithiation Ni oxidizes first, followed by Co, while Mn remains inactive.[29] They also showed the oxide retains its O3 structure on complete delithiation, which is in accord with the experimental findings of Jung and coworkers.[30] Aurbach et al. noted that doping NCM523 with small amounts of Al improves capacity retention and lowers charge transfer resistance at the oxide-electrolyte interface.[31] Performance improvements were also noted by Lee et al. who used 5 wt% methyl (2,2,2 trifluoroethyl)carbonate (FEMC) in a 1 M LiPF$_6$ ethylene carbonate (EC):ethylmethyl carbonate (EMC) (3:7 v/v) electrolyte.[32] Substituting some of the Li with Na to yield $(Li_{0.97}Na_{0.03})Ni_{0.5}Co_{0.2}Mn_{0.3}O_2$ is also reported to improve performance by producing a well-ordered α-NaFeO$_2$ structure with a lower degree of cation mixing and rapid Li$^+$ diffusion in the oxide bulk.[33]

All studies listed in the previous paragraph were conducted in cells with a lithium-metal counter electrode. Here we describe electrochemical cycling studies conducted in full cells with a NCM523-based positive electrode and a capacity-matched graphite-based negative electrode. Several hundred cells containing this NCM523//Gr electrode couple have been examined in various cell configurations and under various test conditions. In this article we report performance data from full cells that underwent up to ∼400 cycles between 3.0 and 4.4 V. We interweave data from electrodes harvested from the cycled cells to identify causes of cell performance degradation, which include capacity fade and impedance rise. From an analysis of differential voltage plots we note the shifts in electrode potential windows that result from cell cycling. We describe X-ray photoelectron spectroscopy (XPS) and secondary ion mass spectroscopy (SIMS) data obtained on positive and negative electrode samples and highlight the effects of cell aging on electrode surface films. We conclude that the electrochemical aging trends, and the electrode surface films on aging, are similar to those of other layered oxide full cells that we have examined previously. In upcoming articles we'll describe results of other physicochemical diagnostic studies conducted on the cell components and will provide suggestions to minimize performance degradation.

*Electrochemical Society Member.
[z]E-mail: abraham@anl.gov

Table I. Electrode composition and constitution.

Negative Electrode (aka Gr)	92 wt% graphite (Phillips 66, A12)
	2 wt% C-45 (Timcal)
	6 wt% PVdF (KF-9300, Kureha)
	Cu current collector (10 μm)
	Coating thickness: 44 μm
	Porosity: 38.4 %
	Active* loading: 5.51 mg/cm^2
Positive Electrode (aka NCM523)	90 wt% Li$_{1.03}$(Ni$_{0.5}$Co$_{0.2}$Mn$_{0.3}$)$_{0.97}$O$_2$ (TODA)
	5 wt% C-45 (Timcal)
	5 wt% PVDF (Solef 5130, Solvay)
	Al current collector (20 μm)
	Coating thickness: 34 μm
	Porosity: 33.5 %
	Oxide loading: 8.25 mg/cm^2

*Active includes graphite and C45.

Experimental

Materials and electrodes.—All electrodes examined in this article are from the Cell Analysis, Modeling and Prototyping (CAMP) facility at Argonne. Table I shows the chemistry and formulation of the electrodes. In addition to the NCM523 oxide (from TODA America), the positive electrode coating also contained C45 carbon black for improved electronic conductivity and PVdF binder for coating cohesion and adhesion to the Al current collector. The negative electrode coating contained A12 graphite (Phillips 66), C45 carbon black, and PVdF binder. Representative SEM images of the NCM523 oxide and A12 graphite are shown in Figure 1. The NCM523 secondary particle has a spherical morphology and contains primary particles that are tightly packed together. Size analysis showed secondary particles in the 6 to 20 micron range with a mean diameter of about 12 microns; the primary particles ranged in size from 0.2 to 2 microns. The graphite particles are carbon-coated and display a potato-shaped morphology; the particles are in the 4 to 19 micron size range and have a mean diameter of about 11 microns. All cells also contain the EC:EMC (3:7 by wt) + 1.2 M LiPF$_6$–based (Gen2) electrolyte and Celgard 2325 trilayer separator.

Electrochemical examination of full cells.—Electrochemical tests were conducted with MACCOR cyclers on 2032-type (Hohsen) coin cells assembled in an argon-atmosphere glove box. The positive and negative electrode areas were the same (1.58 cm^2); all electrodes were dried for at least 3 hours in a vacuum oven at 110°C prior to cell assembly. The assembled cells were tested in a constant-temperature chamber held at 30°C. Initial tests were conducted with various cycling currents to determine the rate-properties of the electrochemical couple; the 1C capacity of the cells, determined for the 3.0–4.4 V voltage window, was ∼1.53 mAh/cm^2 (or 177 mAh/g-oxide). Hence-

forth, all current and capacity values quoted in this article as mA/g or mAh/g refer to grams (g) of oxide in the positive electrode. The C-rates quoted are based on the 1C capacity value shown above.

Long-term cycling tests were conducted in the 3.0–4.4 V range. The tests included four formation cycles at a ∼C/10 rate, followed by aging cycles at a ∼C/3 rate that included a 3-h constant voltage hold at 4.4 V. This constant current-constant voltage (CC-CV) cycling test was interrupted periodically to obtain reference performance data, which included impedance measurements using a modified hybrid pulse power characterization (HPPC) protocol and capacity measurements at low rates (∼C/20) to determine the true loss of cyclable lithium. AC impedance data were obtained after formation cycling and periodically during cell aging. The data were collected on a Solartron Analytical 1470E cell test system in the 100 kHz to 5 mHz frequency range with 10 measurements per decade and a 5 mV rms potential perturbation from the open circuit potential.

Electrochemical examination of harvested electrodes.—Throughout the aging tests selected coin cells were removed at predetermined intervals for detailed diagnostic evaluation. Before disassembly the cells were cycled between 3.0–4.4 V at a very slow rate (typically <C/50), then held at 3.0 V for at least 12 h. Cell disassembly was conducted in an Ar-atmosphere glove box and the various cell components were extracted for further examination.

A schematic that describes preparation of cells with the harvested electrodes is shown in Figure 2. To determine effect of aging on electrode capacities, coin cells were assembled with the harvested electrodes, lithium-metal counter electrode, fresh Celgard 2325 separator, and fresh Gen2 electrolyte. The harvested electrodes were *not* rinsed prior to cell assembly; rinsing with solvents such as DMC is known to reduce capacities of harvested positive electrodes, while increasing capacities of the harvested negative electrodes.[34] Cells containing the positive electrode were cycled from 3.0 to 4.5 V vs. Li/Li$^+$, and cells containing the negative electrode from 1.5 to 0.005 V vs. Li/Li$^+$, with very low currents (typically <C/50 rate). Because of the very low currents, the effect of impedance could be neglected, and the measured capacities can be assumed to reflect the true capacity of the electrodes.

To determine effect of aging on electrode impedance the following procedure was used (also see Figure 2). First, full cells with the pristine electrodes were prepared and subjected to formation cycling (4 cycles, 3–4.4 V, 30°C). The cells were then disassembled and electrodes harvested – these are referred to as the "formed" electrodes. The "aged electrodes" were harvested from cells described in the previous paragraph, that is, from half cells containing the aged electrodes that were cycled to determine cell capacity. Note that these aged cells were cycled once so that the positive electrode is now "relithiated" and the negative electrode is "delithiated". The Aged(+) (Aged-Positive) and Formed(−) (Formed-Negative) electrodes were coupled, and the Formed(+) (Formed-Positive) and Aged(−) (Aged-
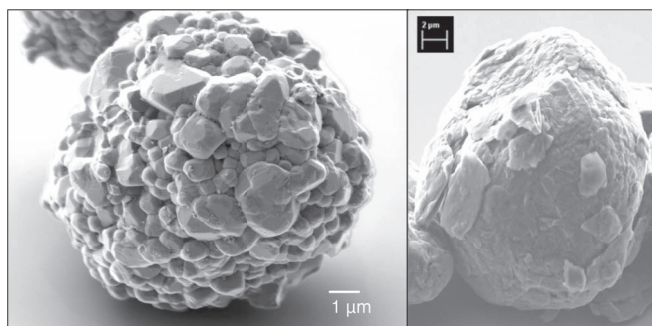

Figure 1. SEM images of an NCM523 oxide secondary particle (left) used in the positive electrode and a graphite particle (right) used in the negative electrode.
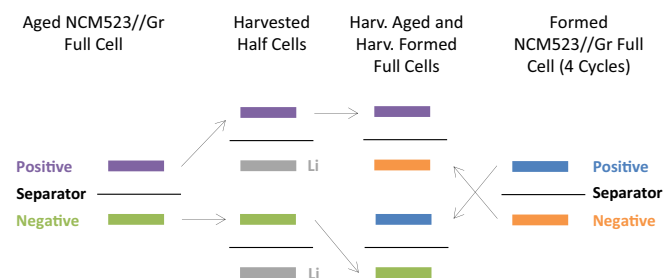

Figure 2. Schematic showing preparation of cells with the harvested electrodes for capacity and impedance measurements. For capacity determination the harvested electrodes are incorporated into cells with a Li-metal counter electrode (half cells). For impedance determination hybrid cells containing harvested aged electrodes and harvested formed electrodes are assembled. All cells contain Celgard 2325 separator and Gen2 electrolyte.

Negative) electrodes were coupled, to make "hybrid" full cells. To prepare both sets of cells fresh Celgard 2325 separators and fresh Gen2 electrolyte were used. Note that the harvested electrodes were *not* rinsed prior to cell assembly. By comparing data from Aged(+)/Formed(−) and Formed(+)/Aged(−), the relative electrode contributions to impedance rise on cell aging could be determined.

SIMS and XPS studies of fresh and harvested electrodes.—Dynamic SIMS experiments were conducted on pristine and harvested negative electrodes with a Cameca IMS-5F system using a 12 kV O_2^+ primary ions and a beam current of 100 nA; the O_2^+ primary ions were used to enhance signals from the metal constituents. In SIMS, samples bombarded with the energetic primary ions eject secondary atoms and ions from the top layer of surface molecules; the ejected ions are subsequently accelerated into a mass spectrometer, where they are separated and counted based on their mass-to-charge ratio.[35] Positive secondary ions were detected and analyzed in our experiments. The elemental depth profiles were obtained with a raster size of $250 \times 250\,\mu$m and an image field of $150\,\mu$m; data for each element was collected for one second before switching to the next one.

XPS data were obtained on electrode samples with a PHI 5000 *VersaProbe II* system from Physical Electronics, with a base pressure $\sim 2 \times 10^{-9}$ Torr. The system is attached to an Ar atmosphere glove box and the samples were inserted into the XPS analysis chamber through the glove box, without exposure to ambient air. All harvested electrode samples were lightly rinsed in DMC before analysis to remove electrolyte residue. The spectra were obtained using an Al $K\alpha$ radiation (hυ = 1486.6 eV) beam (100 μm, 25 W), Ar$^+$ and electron beam sample neutralization, and Fixed Analyzer Transmission mode. Peak fits of all spectra were performed using the Shirley background correction and Gaussian-Lorentzian curve synthesis available in the CASAXPS software. For the positive electrodes the energy scale was adjusted based on the 285.0 eV carbon peak in the C1s spectra. For the negative electrodes the adjustment was based on the graphite peak in the C1s spectra at 284.5 eV; for samples that did not show a distinct graphite peak the adjustments were based on those of a pristine electrode examined under the exact acquisition conditions.

Results and Discussion

Capacity and capacity fade – full cell and Harvested electrode data.—A representative example of capacity-voltage plots from the NCM523//Gr full cells is shown in Figure 3; values of the capacity, capacity fade, coulombic efficiency, energy, energy fade, energy efficiency, and average voltage derived from the plots are shown in Table II. For the first cycle, the charge and discharge capacities are 217.6 and 189.2 mAh/g respectively, yielding a CE of 87.0%. At cycle 404, values of the discharge capacity, capacity fade, and coulombic efficiency are 112.5 mAh/g, 40.5%, and 99.4%, respectively; the corresponding values of the discharge energy, energy fade, and energy efficiency are 433 mWh/g, 39.4%, and 97.7%, respectively. Note that the energy efficiency is lower than the coulombic efficiency after the initial cycles,
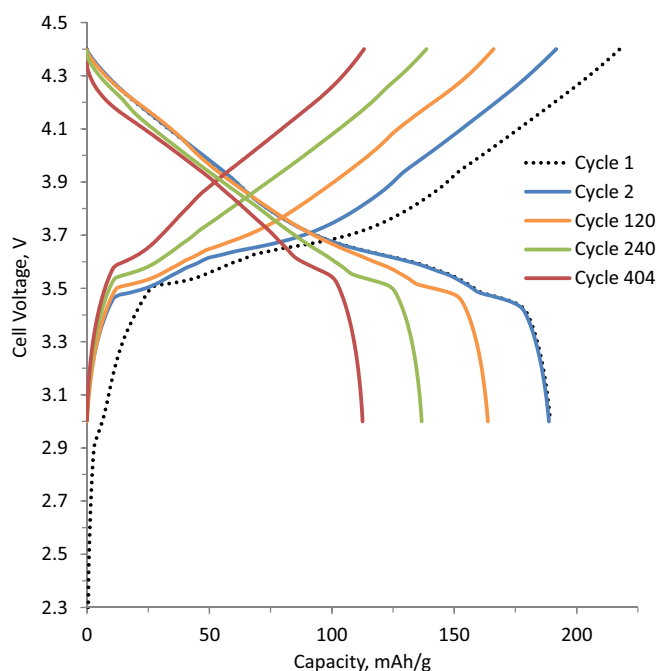

Figure 3. Capacity-voltage profiles for NCM523//Gr cells as a function of aging for the various cycles (3.0–4.4 V, 30°C), indicated in the plot.

indicating a small degree of voltage hysteresis between the charge and discharge cycles. The average cell voltage during the discharge cycle also increases, which indicates a shift of the cell capacity to higher voltages; this trend is different from the voltage *fade* trends observed in the lithium- and manganese-rich layered oxides.[17]

The loss in capacity on cycling is also evident in Figures 4a and 4b. Figure 4a shows a representative discharge capacity plot as a function of cycle number; note that cell capacities were obtained with various currents during aging. Salient observations from Figure 4a are as follows: (i) cell capacities obtained with higher currents (180 mA/g) are lower than the capacities obtained at lower currents (e.g. 60 mA/g), which is a reflection of the cell impedance; note that these capacity differences are not uniform during cycling; (ii) capacity of the final cycle (404) was measured with a very low current (3.6 mA/g); no "additional" capacity was obtained at this current compared to the value determined with the 60 mA/g current, indicating a true loss of cyclable lithium ions.

Figure 4b shows the capacity loss, calculated for two currents, 18 mA/g and 180 mA/g. The values are the average of multiple cells tested under the same conditions; the error bars reflect variations in the data obtained from multiple cells. Note that the capacity variation between cells at the low current is small. At higher currents, the variation is small initially, but increases on cycling and is significant beyond ∼200 cycles. The percent capacity loss measured with the lower current is linear, ∼40% capacity loss after 404 cycles. Because this value roughly reflects the amount of cyclable lithium, the data indicates that the lithium loss is a linear function of the cycle number. At the higher current, the measured percent capacity loss is not linear indicating a greater influence of cell impedance, especially beyond ∼200 cycles. Cell-to-cell variations and the greater influence of impedance during extended cycling suggest that we should be careful about extrapolating short-term capacity data, especially those obtained at higher C-rates, to longer-term periods.

In order to determine electrode contributions to cell capacity fade we obtained capacity data on electrodes harvested from cells after formation cycles and after extended cycling. Because of the very low currents, the effect of impedance can be neglected and capacities measured can be assumed to reflect the true capacity of the electrodes. Figures 5a and 5b show data from the positive and negative elec-
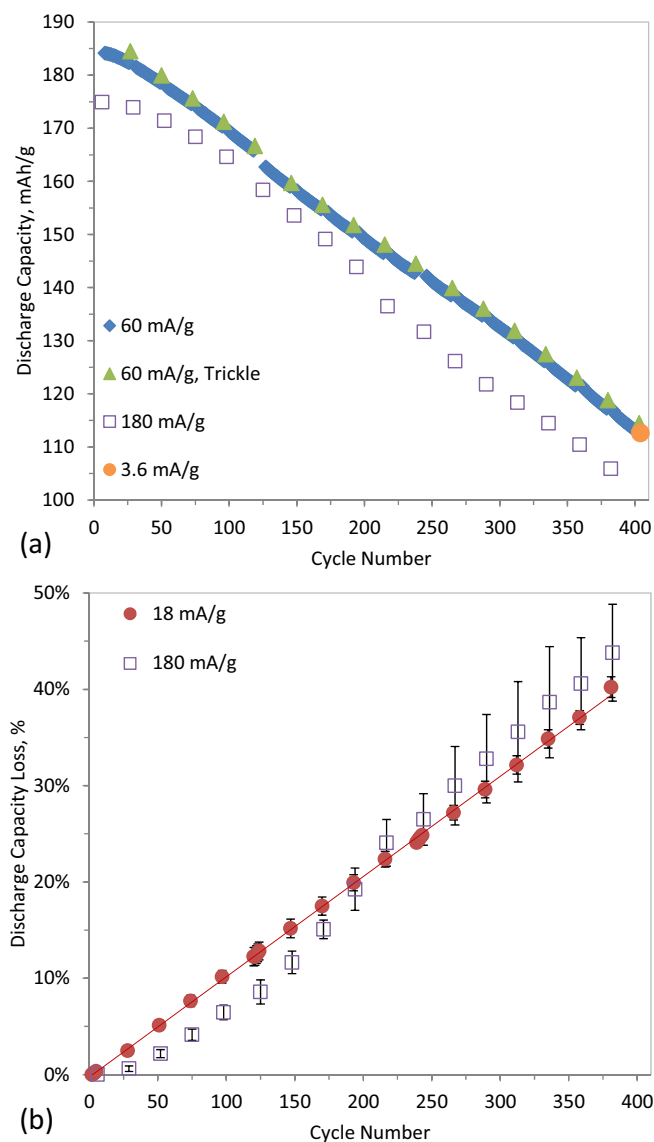
Table II. Data associated with Figure 3 (NCM523//Gr, 3.0–4.4 V, 30°C) showing charge (C) and discharge (D) capacities, coulombic efficiency (CE), discharge capacity fade (DCF), charge energy (CE), discharge energy (DE), energy efficiency (EE), discharge energy fade (DEF), and average voltage on discharge (AVD), of the various cycles.

Cycle	C mAh/g	D mAh/g	CE %	DCF %	CE mWh/g	DE mWh/g	EE %	DEF %	AVD Volts
1	217.6	189.2	87.0	0.0	819	714	87.2	0.0	3.772
2	191.7	188.7	98.4	0.3	729	712	97.7	0.3	3.773
120	166.1	163.7	98.6	13.5	637	623	97.7	12.8	3.803
240	138.7	136.7	98.6	27.8	537	522	97.3	26.8	3.822
404	113.2	112.5	99.4	40.5	443	433	97.7	39.4	3.845

Figure 4. (a) Discharge capacity trends for NCM523//Gr cells as a function of cycling (3.0–4.4 V, 30°C) for currents of 3.6 mA/g, 60 mA/g, 60 mA/g with a trickle discharge down to 9 mA/g, and 180 mA/g. (b) Average discharge capacity loss for two currents, 18 mA/g and 180 mA/g.

Figure 5. Cell voltage profiles (<C/50, 30°C) for (a) the NCM523//Li cell cycled between 3.0 and 4.5 V and (b) the Gr//Li cells cycled between 1.5 and 0.005 V. The electrodes were harvested from full cells after formation cycling, 120 cycles, 240 cycles, and 404 cycles.

trodes, respectively. The discharge capacity of the positive electrodes harvested from cells after formation cycling, 120 cycles, 240 cycles and 404 cycles are 202, 199, 197 and 189 mAh/g-oxide, respectively; the corresponding values for the harvested negative electrodes are 354, 345, 344 and 330 mAh/g-graphite, respectively. These data indicate that both positive and negative electrodes lose some capacity after extended cycling – these losses may arise from various factors that include particle isolation resulting from fracture and/or loss of electronic connectivity, loss of electrode active material through dissolution into the electrolyte, and reductions in specific capacity because of phase changes in the active materials.

Additional information on electrode contributions to cell capacity fade can be obtained from an analysis of differential voltage (dV/dQ) plots derived from the full cell data.[36–38] From inspection of the positive and negative electrode half-cell plots obtained at low currents (<C/20 rate), peaks in the dV/dQ plots of the full cell data, also obtained at low currents, can be assigned; these peaks arise from phase transitions in active materials of the electrodes. The positions of these peaks shift as the full cell ages, depending on the capacity loss mech-
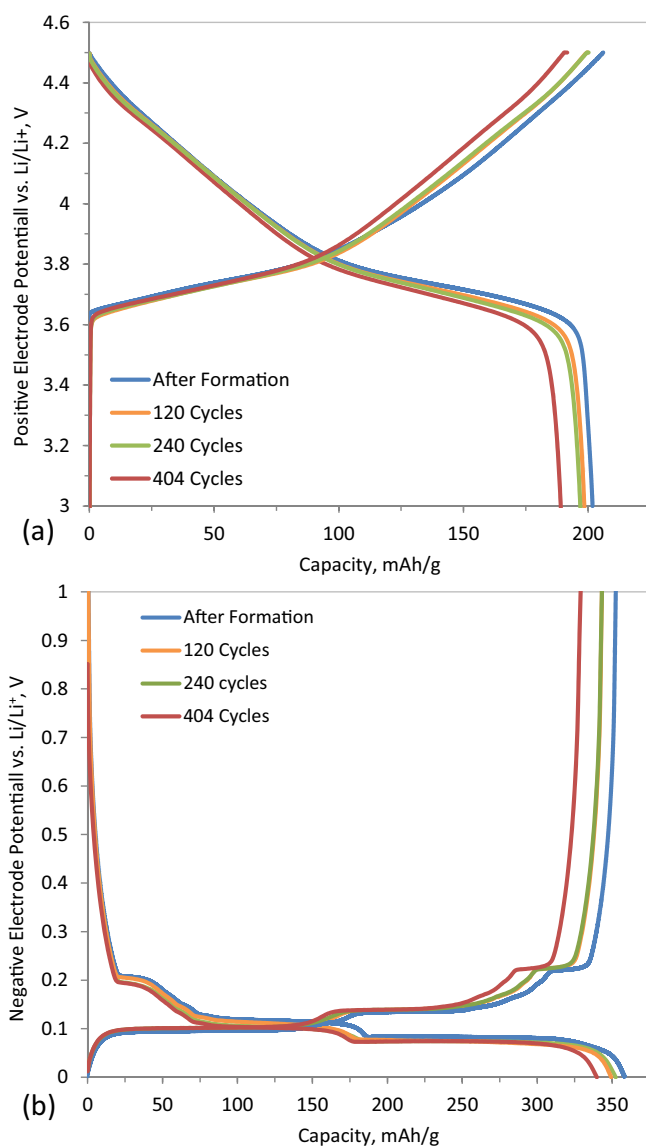
anism(s). To fit the new peak positions the electrode half-cell data can be shifted relative to each other to account for side-reactions in the cell, and can be shrunk (or expanded) to account for the loss (or gain) of active material.

Figure 6 shows the positive and negative electrode potential shifts obtained from fitting dV/dQ curves collected on NCM523//Gr cells after formation cycling, 120 cycles, 240 cycles, and 404 cycles in the 3.0–4.4 V range; the full cell data is shown for comparison. Note that the electrode voltage profiles are from cells containing a Li-metal counter electrode after formation cycling and were obtained at a <C/50 rate. The same voltage profiles are used for all cycles. We could fit the dV/dQ curves by simply shifting the electrode plots relative to each other and without expanding or shrinking the curves. That is, the electrode potential shifts result from net-reductive side-reactions in the cell, and not from a loss of electrode active material. It is evident from Figure 6 that the formation cycling induces electrode potential window shifts and that extended cycling increases the magnitude of these shifts, almost linearly with the cycle number. The shifts reduce utilization of active material in both positive and negative electrodes.
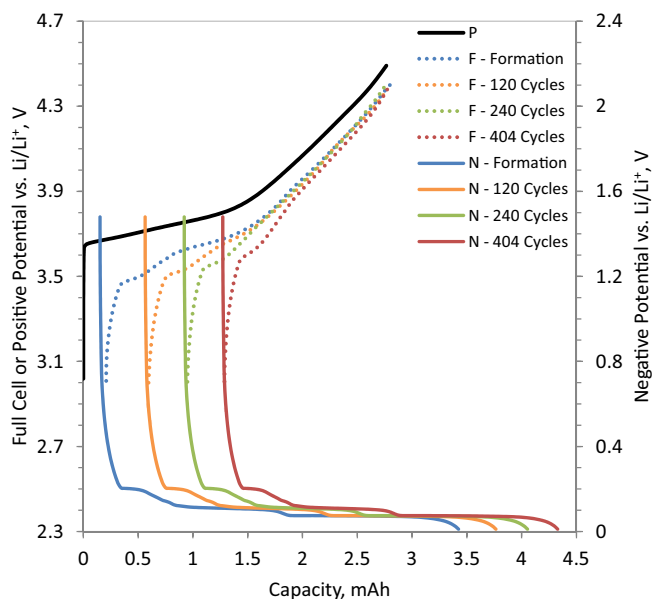
Figure 6. Electrode potential shifts in NCM523//Gr full cells after formation cycling, 120 cycles, 240 cycles, and 404 cycles between 3.0 and 4.4 V as determined through dV/dQ analysis. In the legend P, N and F refer to the positive electrode, negative electrode, and full cell, respectively.

The reduction is far greater than the capacity losses determined from the harvested electrode studies; i.e., the contribution of active material isolation to cell capacity loss is minimal compared to capacity loss resulting from undesired side reactions. In addition Figure 6 shows that the electrode potential window shifts cause the positive electrode to cycle at higher states-of-charge as aging progresses, which could accelerate degradation at the electrode.

Impedance and impedance rise – full cell and harvested electrode data.—Cell impedance is an importance measure for transportation applications because batteries may be discharged rapidly during vehicle acceleration or charged rapidly during vehicle (regenerative) braking.[39] Because both acceleration and braking demand high current bursts during short time periods the impedance is often determined by the hybrid pulse power characterization (HPPC) test which measures the cells' ability to withstand high discharge or charge current pulses without significant degradation.

In a typical HPPC test, the cell is charged to its upper cutoff voltage (UCV, 4.4 V in this study), then subjected to repetitions of a pulse profile that contains 10% depth of discharge (DOD) constant-current C/1 discharge segments followed by a 1 h rest period and constant-current discharge (2C, in this study) and charge (1.5C, in this study) 10-second pulses.[40,41] Note that the C/1 currents used are based on the initial capacity of the cell; the 10% DOD segments between the current pulses are *not* adjusted to reflect the capacity of the aged cell. In addition, upper and lower voltage limits are set for the HPPC test to prevent overcharge or overdischarge of the cell; here, the limits are at 4.5 V and 2.5 V, respectively. Area specific impedance (ASI) values are calculated from the cell voltage change during the current pulses; the geometric area of the electrode is used for this calculation because the actual electrochemical area that contributes to the measured currents is a very difficult parameter to measure accurately.

A representative example of ASI values during the discharge pulse from an NCM523//Gr cell, as a function of cell voltage and cycle number is shown in Figure 7a. It is evident that cell impedance increases on cycling; furthermore the impedance rise is non-uniform across the voltage range and is higher for cell voltages >4.0 V. Note that the actual voltages of the current pulse are indicated by the markers. After formation cycling (marked as cycle 7), data from nine discharge pulses are obtained during the measurement. As cycling progresses
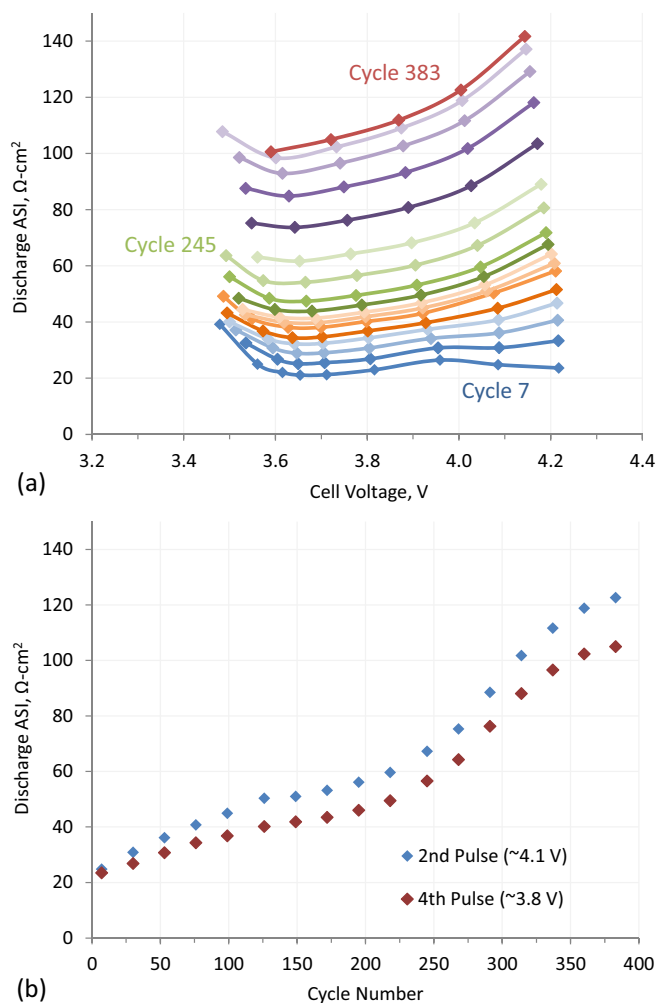

Figure 7. (a) Area specific impedance (ASI), calculated from HPPC tests on a NCM523//Gr full cell, as a function of cell voltage and cycle number. (b) ASI as a function of cycle number for the 2nd (∼4.1 V) and 4th (∼3.8 V) pulses.

and cell impedance rises, fewer and fewer data points are obtained as the cell is unable to complete the high current pulses because of the lower voltage limit set to prevent overdischarge. Thus after 126, 245 and 383 cycles the ASI values are only obtained at 8, 7 and 5 voltage locations, respectively.

The ASI values at the 2nd and 4th discharge pulse, as a function of cycle number, are shown in Figure 7b; the *nominal* cell voltages at these pulse locations are ∼4.1 V and ∼3.8 V, respectively. Some relevant features from the plots are as follows: (i) the ASI increases at both pulse locations are not linear – the rise is gradual initially (up to ∼220 cycles), then relatively rapid, then gradual again; such a trend in impedance rise has been observed previously for NCA/Gr cells;[34] (ii) although similar initially, the ASI values at the 2nd discharge pulse (the higher of the two full cell voltages plotted) increases faster and always remains higher than the values at the 4th discharge pulse.

Additional information on cell impedance rise was obtained from AC impedance spectroscopy.[42–44] Representative AC impedance plots from a NCM523//Gr cell as a function of cell cycling is shown in Figure 8; the data were obtained in the 100 kHz–0.005 Hz frequency range at full cell voltages of (a) 3.8 V and (b) 4.1 V. Note that the measured data result from a superposition of several mechanistic processes at both the positive and negative electrodes.

A typical plot in Figure 8 contains a partially-formed arc (A$_1$) at higher frequencies, a depressed arc (A$_2$) at mid-frequencies, and a Warburg impedance tail at low frequencies. The inset tables list the frequencies at the locations defined in Figure 8a – f$_1$ is the frequency
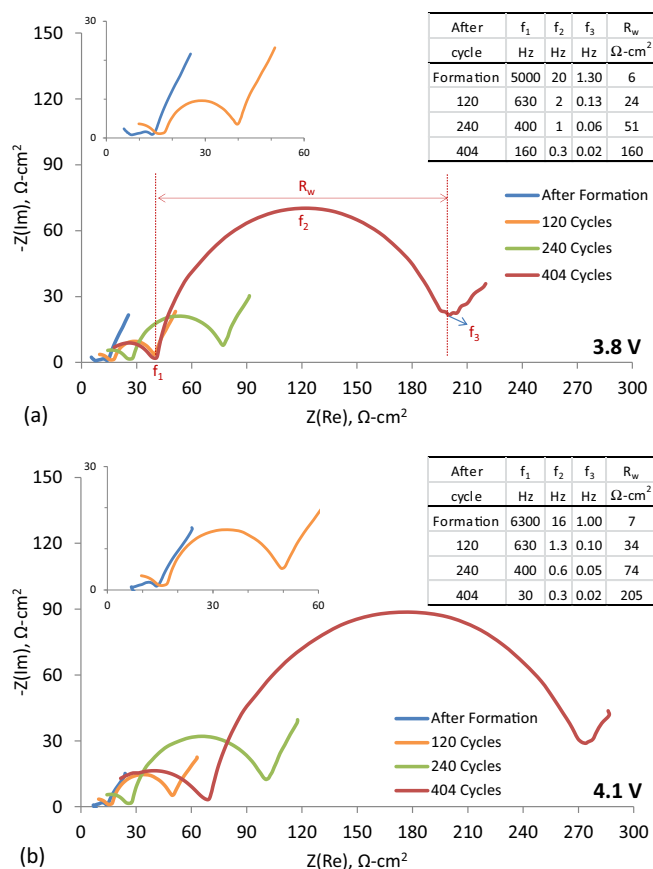
Figure 8. Representative full cell AC impedance plots as a function of cycling. The data were obtained at 30°C, at a full cell voltage of (a) 3.8 V and (b) 4.1 V, in the 100 kHz to 0.005 Hz frequency range. For clarity, the inset figures show expanded views of data from cells after formation cycling and after 100 cycles. The inset table details frequencies (f_1, f_2, f_3) at locations defined in (a) and lists width of the mid-frequency arc (R_w).
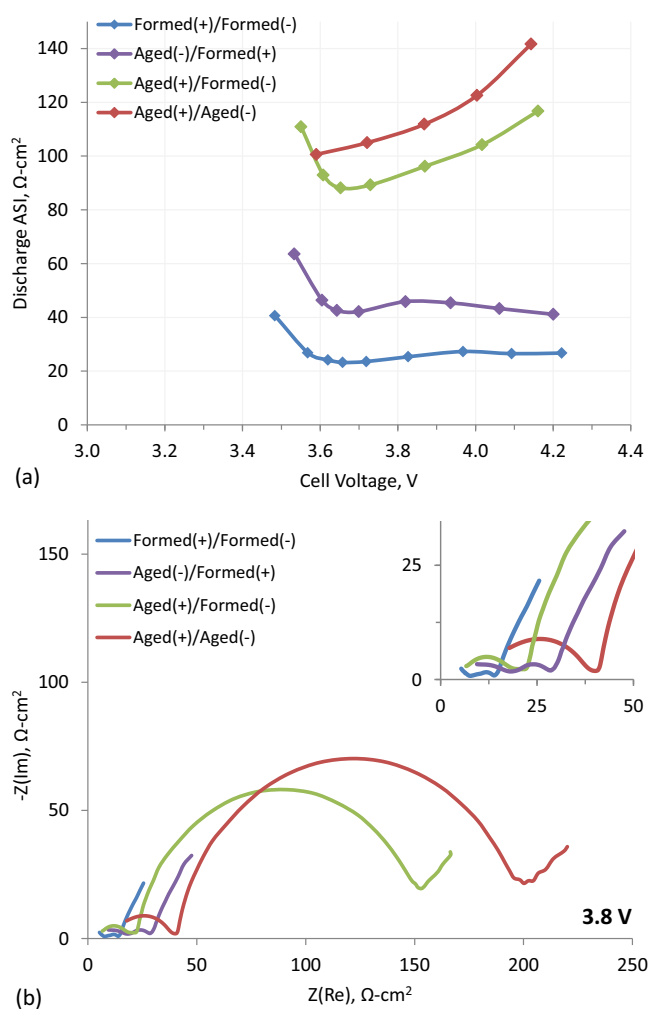

Figure 9. Area specific impedance (ASI) data obtained from HPPC (a) and AC impedance (3.8 V, 100 kHz - 0.005 Hz, 30°C) experiments (b). Electrodes were harvested from Formed (4 cycles, 3–4.4 V) and Aged (404 cycles, 3–4.4 V) cells. The inset in (b) shows an expanded view of the data.

at the intersection of arcs A_1 and A_2, f_2 is the frequency at the maximum value of A_2 along the Y-axis, and f_3 is the frequency at the intersection of arc A_2 and the Warburg tail. The tables also list the width of the mid-frequency arc (R_w), defined as the resistance difference (i.e., along the X-axis) between f_1 and f_3. The main observations from Figures 8a and 8b are as follows: (i) the frequencies (f_1, f_2, f_3) decrease on aging. For example in Figure 8a, f_3 decreases by almost two orders of magnitude from 1.3 Hz after formation cycling to 0.02 Hz after 404 cycles. Because the frequency values are inversely proportional to time constants of electrochemical processes, the data indicate that the cell kinetics slows down on aging; (ii) the value of R_w increases on aging. For example, in Figure 8a (3.8 V), R_w increases from 6 Ω-cm² after formation cycling to 160 Ω-cm² after 404 cycles. The corresponding increase in Figure 8b (4.1 V) is from 7 Ω-cm² to 205 Ω-cm² – it is evident that the R_w increase is greater at 4.1 V, consistent with trends observed in the HPPC data; (iii) impedance at the 100 kHz point increases on aging. For instance, in Figure 8a (3.8 V) the Z(Re) value increases from 5 Ω-cm² after formation cycling to 18 Ω-cm² after 404 cycles.

Additional information on cell impedance rise on aging is obtained from examining data from the harvested electrodes. Representative examples are shown in Figure 9, which contains data from HPPC (9a) and AC impedance (9b) experiments. Figure 9a shows four plots showing the discharge ASI as a function of cell voltage. As expected, the Formed(+)/Formed(−) cell shows the lowest impedance while the Aged(+)/Aged(−) cell shows the highest impedance. In between are profiles from the "hybrid" cells, i.e., the Aged(+)/Formed(−) and Formed(+)/Aged(−) cells. It is evident that the impedance of the

Aged(+)/Formed(−) cell is much larger than the impedance of the Formed(+)/Aged(−) cell. We may hence conclude that during cell aging the positive electrode is the main contributor to cell impedance rise; the negative electrode impedance does increase but its contribution to the full cell impedance is smaller. This result is in accord with observations from other cells containing layered oxide-based positive electrodes and graphite-based negative electrodes.[5,34] Another observation from Figure 9a is that the "hybrid" cell plots contain data at more voltage locations than the aged cell; these additional data points are obtained because the hybrid cells contain a "relithiated" positive and a "delithiated" negative electrode, as described in the Experimental section.

The AC impedance plots (Figure 9b) also show that the impedance of the Aged(+)/Formed(−) cell is much larger than the impedance of the Formed(+)/Aged(−) cell. Furthermore, it is evident that the positive electrode is the main contributor to growth of both arcs A_1 and A_2 on cell aging. We have previously attributed the growth of arc A_1 to an "electronic" impedance that may arise at the oxide-carbon interface or at the coating-current collector interface.[5,45] Because there was no obvious sign of positive electrode delamination during cell disassembly we posit that the growth of arc A_1 results from increasing impedance at the oxide-carbon interface. This conclusion is in accord with a recent FIB-SEM serial sectioning study on cycled NMC-based electrodes by Liu et al., which indicated detachment of the carbon-doped binder from the active oxide particles.[46] The growth of this arc

can hence be minimized by altering electrode fabrication conditions, which includes optimization of the oxide/carbons/binder ratios used for electrode preparation.[47] Arc A_2 was characterized earlier by R_w (mid-frequency arc width), which can be attributed to impedances at the oxide-electrolyte interface.[42] Contributors to R_w increase include surface films that form at the oxide-electrolyte interface because of electrolyte decomposition, alterations to the oxide-surface crystal structure, separation of primary particles, etc.

Other salient observations from Figure 9b include the following: (i) the Z(Re) value at the 100 kHz point for the hybrid cells is similar to that of the Formed(+)/Formed(−) cell. Because the hybrid cells contain fresh separators and electrolyte it's possible that the small impedance rise at this frequency location for the aged cell (noted above) may reflect increases in electrolyte resistance and/or resistances arising from separator clogging;[48] (ii) the small negative electrode impedance growth is seen as an increase in the mid-frequency arc width and increase in the diffusion tail length. Both increases reflect changes in the SEI layer (shown later) that affect lithium-ion transport in and out of the active graphite particles.

SIMS studies of fresh and harvested negative electrodes.—In the past we have used the SIMS technique to examine accumulation of transition metals at the negative electrodes during electrochemical cycling.[4,5,17,49] SIMS is suitable for this purpose because of its excellent detection limits (ppb to ppm) for transition metal elements and its ability to provide elemental profiles of a sample with good resolution as a function of sputtering depth. Figure 10 shows SIMS sputter depth profiles for carbon, manganese, nickel, and lithium from a pristine negative electrode and from electrodes harvested from cells after formation cycles, 240 cycles and 404 aging cycles. Note that the count rates in dynamic SIMS profiles depend on the ionization efficiency, which varies from element to element. Therefore we cannot draw conclusions about elemental concentrations in samples from the absolute count rates values. However, we can compare data for the same element from different samples because the matrix material is carbon and the counts are similar ($\sim 1.4 \times 10^4$) in the bulk for all samples.

The carbon profile (top-left of Figure 10) of the pristine negative electrode sample serves as a point of reference; the sample contains only carbonaceous species (graphite, C45 carbon, PVdF) and hence displays a fairly constant sputter-depth profile. The profile does not change much after formation cycling but significant changes are seen in the 240 cycle and 404 cycle samples. For these samples, the count rates are low initially and then rise during the sputtering process eventually attaining a steady-state value. For the 240 cycle and 404 cycle samples the time required for the C-signal to reach levels similar to that of the pristine material are $\sim$350 s and $\sim$2000 s, respectively. The longer sputtering times suggest a thicker SEI and/or an SEI that sputters slower when bombarded with the O_2^+ primary ions. These observations are consistent with the XPS data (described later) which indicate that the negative electrode SEI progressively becomes *inorganic*, i.e., the SEI carbon content decreases, while the fluorine, phosphorous and lithium content increases on extended cycling.

Aging-related changes are also seen in the Mn (top-right in Figure 10) and Ni (bottom-right) profiles collected on the harvested electrodes. Only trace quantities of these elements are present in the pristine electrode and hence the corresponding count rates are very low and not shown in the plots. In the Mn profiles, the formation cycle sample shows an elevated count rate near the surface ($\sim$310 cps), which decreases on sputtering and eventually attaining a steady-state value ($\sim$130 cps) in the sample bulk. On the other hand, higher values are seen for the 240 cycle ($\sim$1100 cps) and 404 cycle ($\sim$7000 cps) samples at longer sputtering times, indicating a higher Mn content in the sample bulk. The differences are even more distinct in the near surface regions. For example, the highest count rates in the Mn profile of the 240 and 404 cycle samples (seen at shorter sputtering times) are $\sim 1.0 \times 10^4$ cps and $\sim 1.7 \times 10^5$ cps, several orders of magnitude higher than the $\sim$310 cps seen for the formation cycle sample. In the Ni profiles, the differences are mainly seen at longer sputtering times,

wherein the aged sample counts are about five times greater than those of the sample after formation cycling.

A conspicuous feature is the maximum peak values seen in the Mn and Ni profiles. This maximum results from increasing count rates during the initial phase of sputtering and may represent the time taken for the near-surface oxygen concentrations to reach equilibrium.[35] Alternatively the data may indicate that these elements are buried under an overlying SEI layer. Such a layer is expected because the transition metals are expected to serve as centers for enhanced electrolyte reduction trapping Li^+ in the SEI during the process and, thereby, accelerating cell capacity fade.[50] Note that maximum values are also seen in the Li profiles of the aged samples. For Li, the relatively high count rates, even in the sample bulk, can be attributed to electrode residue left behind after the light DMC-rinse step.

XPS studies of fresh and harvested electrodes.—In XPS the energy of photoelectrons ejected when the sample is irradiated by soft X-rays (Al $K\alpha$, in this study) is analyzed. The unique binding energies and the small escape depths (< 5 nm) of ejected photoelectrons allow elemental identification with excellent surface sensitivity, which is important when examining the electrode SEI. Here we first describe data from fresh and harvested negative electrodes and then the data from fresh and harvested positive electrodes.

Data from the negative electrodes.—Figure 11 displays the C1s, O1s, F1s, Li1s, P2p and Mn3p spectra from a pristine negative electrode and from electrodes harvested from discharged cells after formation cycling and after 404 aging cycles; elemental concentrations are also shown in the included table. The main change observed on extended cycling is the significant reduction in the carbon concentration and corresponding increases in the lithium, fluorine, phosphorous and oxygen concentrations. That is, the negative electrode SEI becomes more *inorganic* during the extended cycling.

A typical C1s spectrum from a pristine negative electrode (Figure 11) shows peaks associated with graphite (C-C) and the PVdF (C-H, C-F) binder, as expected. After formation cycling the graphite peak intensity decreases, while additional intensities are seen at $\sim$285.5 eV (C-H) and $\sim$287.0 eV (C-O); these intensities arise from solvent reduction that leads to generation of SEI species on the electrode.[51] After 404 cycles the peaks associated with the graphite and PVdF binder are no longer seen indicating that these components are buried under a thick SEI. The C1s spectrum intensities are relatively small with intensities centered near 285.9 eV, 287.2 eV and 290.0 eV, which are consistent with the presence of alkoxide (ROLi) and alkyl carbonate ($ROCO_2Li$) species.

The F1s spectrum from a pristine negative electrode shows the C–F peak from the PVdF binder at 687.8 eV. After formation cycling, additional intensities are seen with peaks at 688.4 eV and 686.2 eV; the former peak contains contributions from the C–F bond in the binder and PF_z species, and the latter peak contains contributions from LiF and PO_yF_z species in the SEI. After 404 cycles the peaks associated with the PF_z species decrease, while the peaks associated with the LiF and PO_yF_z species show a significant increase. Corresponding changes are also seen in the P2p spectra and the increasing P content is also evident in the included table.

The O1s spectrum of the pristine negative electrode shows a small amount of oxygen (0.3 at%) that is presumably adsorbed on the electrode surface. The value increases to 11.1 at% after formation cycling with the intensities arising from products of electrolyte reduction. The oxygen concentration does not increase after 404 cycles even though the P2p spectrum depicts increases in the PO_yF_z species. This behavior is in accord with the changing nature of the SEI from more organic (solvent reduction products) to more inorganic (salt reduction/decomposition products) on extended cycling.[52]

Not surprisingly the Li content in the negative electrode SEI increases with cycling, which is consistent with the capacity fade displayed by the cell. As expected only trace amounts of Li are present in the pristine sample. After formation cycling, the higher Li content in the electrode SEI arises from species that result from electrolyte re-
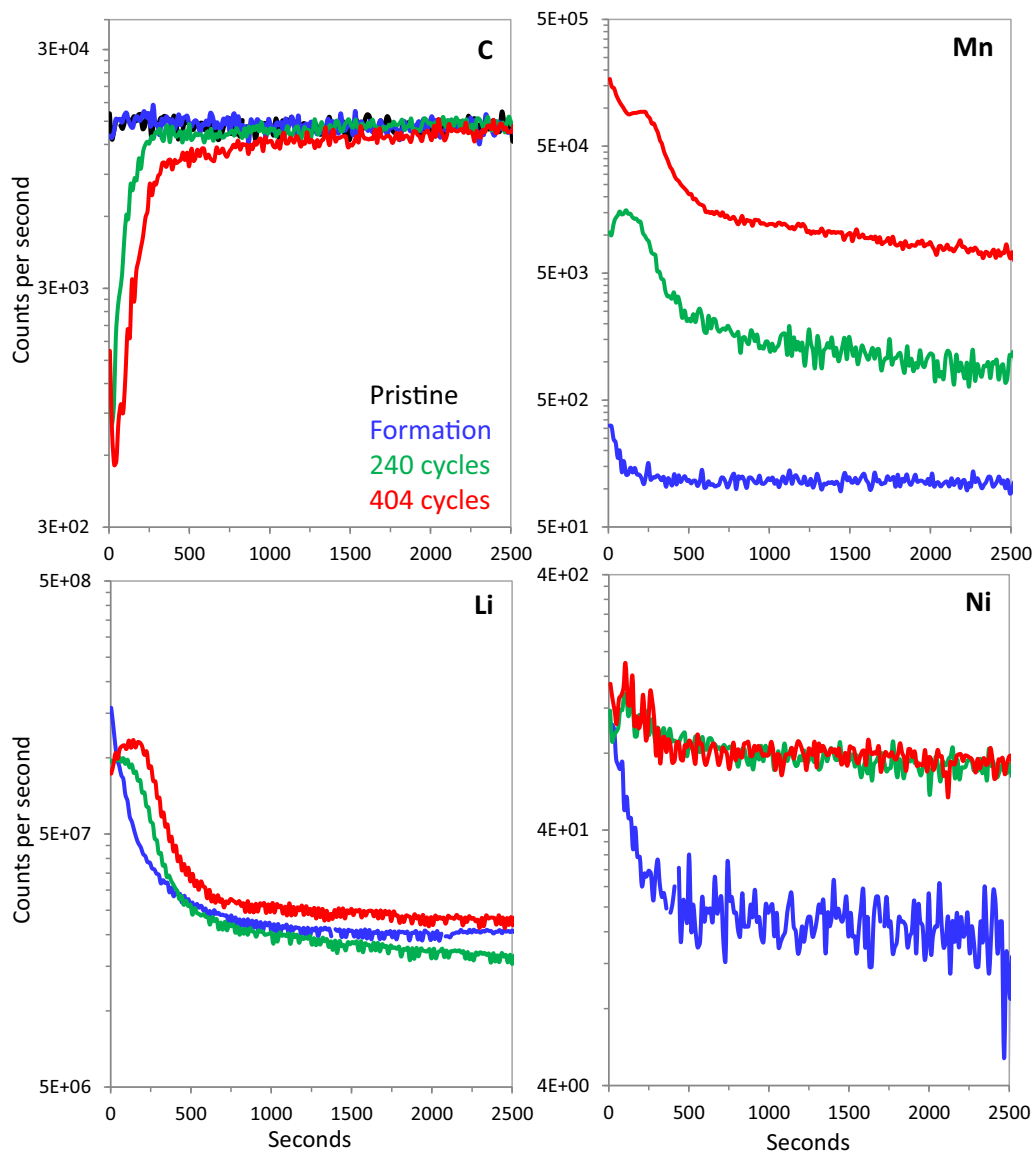
Figure 10. SIMS sputter depth profiles (carbon, manganese, nickel, lithium) from negative electrodes harvested from cells after formation cycles (blue), 240 cycles (green) and 404 cycles (red). Data for the pristine electrode (black) is shown only in the C profiles; Mn, Ni, Li are not present in measurable quantities in the pristine electrode.

duction including Li-bearing organic and inorganic compounds. The measured Li concentration doubles after 404 cycles; the intensities mainly arise from the inorganic species (such as LiF, Li_xPF_z, and $Li_xPO_yF_z$) but some intensities also originate from the ROLi and $ROCO_2Li$ species expected in the SEI. Of particular interest is the Mn3p peak, which indicates that Mn is transported from the positive to the negative electrode during cell cycling, as also indicated by the SIMS data.

Data from the positive electrodes.—Figure 12 displays the C1s, F1s, O1s and P2p spectra from a fresh positive electrode and from electrodes harvested from discharged cells after formation cycling and after 404 aging cycles. For the pristine electrode the C1s spectrum contains contributions mainly from the C45 carbons (285 eV) and PVdF [-$(CH_2CF_2)_x$] binder (286.3 eV, 291 eV); additional intensities observed in the spectra near 289 eV suggest carbonate impurities that likely arise from the oxide surface as seen later in the O1s spectra. After formation cycling intensities of both the graphite and PVdF peaks decrease, indicating the presence of surface films, which are probably inorganic because additional intensities are not seen in the

C1s spectrum. After 404 cycles, however, additional intensities are observed centered around 286 eV, 287.8 eV and 290 eV suggesting the presence of alkyl carbonate species that result from solvent decomposition. Although the graphite and PVdF peak intensities decrease further, they are still clearly visible in the spectrum indicating that the surface films are either thin and/or non-uniform.

Intensity reductions of the PVdF peak are also seen in the F1s spectra. The spectrum of the pristine positive electrode mainly contains a peak centered at 688.5 eV that arises from C-F bonds in the PVdF. Some intensity is also observed around 685 eV, which suggests the presence of LiF that results from the electrode slurry preparation process.[53] After formation cycling additional intensities are observed which are probably from LiF and Li_xPF_z species; the relatively high intensities may indicate that the light DMC rinse was not sufficient to remove all the salt-bearing residue. After 404 cycles, the distinct peak centered near 686.1 eV is mainly from LiF. Salt decomposition species, such as Li_xPF_z and $Li_xPO_yF_z$ species, also contribute to intensities in the 286.5–287.5 eV range. These species are also prominent in the P2p spectra after 404 cycles.
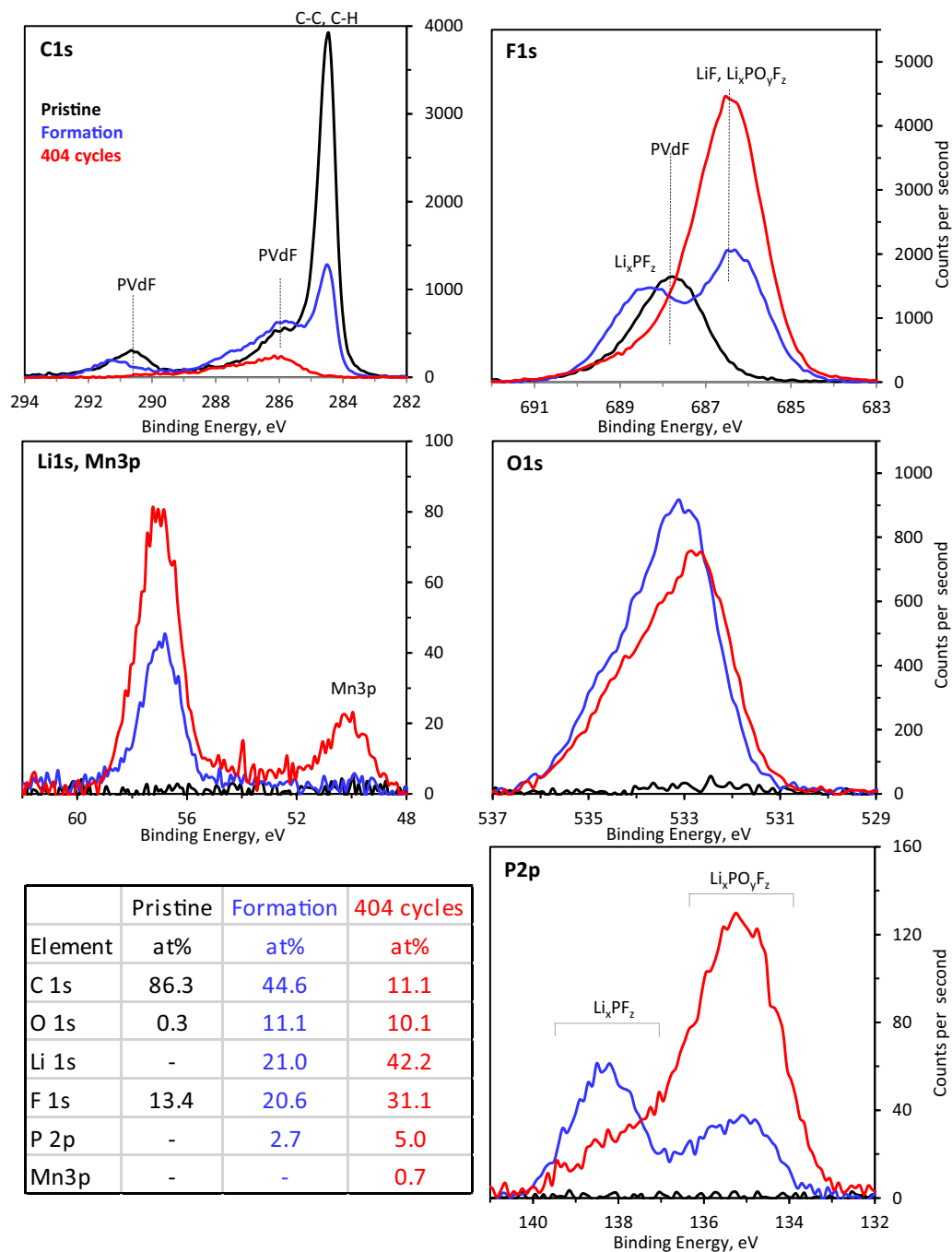
Figure 11. XPS spectra (C1s, O1s, Li1s, Mn3p, F1s, P2p) from negative electrodes harvested from cells after formation cycling (blue) and after 400 cycles (red). Spectra from pristine electrodes (black) are included for comparison. Element concentrations (at%) for the various samples are shown in the table.

In the O1s spectrum of the pristine positive electrode the peak centered at 529.8 eV arises from O^{2-} anions in the NCM523 oxide; another broad peak centered at 532.4 eV can be assigned to surface impurities, such as Li_2CO_3, that have been reported elsewhere.[53] After formation cycling the most distinct feature are the intensities centered at 534 eV, which arise from the products of electrolyte (salt) decomposition;[51] intensity decreases in the 529.8 eV oxide peak and 532.4 eV surface impurity feature are also seen. After 404 cycles the 534.2 eV peak intensity increases significantly and additional intensities centered near 533.5 eV are also seen; these changes are related to the increased alkyl carbonate and phosphate content seen in the C1s and P2p spectra. More importantly, the 529.8 eV oxide peak is still visible after 404 cy-

cles, which indicates that the surface film is thin enough ($\lesssim$5 nm) to allow photoelectrons emitted from the oxide below it to go through.

The positive electrode XPS data may hence be summarized as follows: (i) surface films resulting mainly from electrolyte-salt decomposition are seen after formation cycling; (ii) after extended cycling these surface films, although mainly inorganic, also include products of solvent decomposition; (iii) after 404 cycles electrode components including the oxide, carbon and PVdF are still visible (although at reduced intensities), indicating that the surface films are relatively thin. This result is in striking contrast to the negative electrode data where the SEI completely buries the various electrode components after extended cycling.
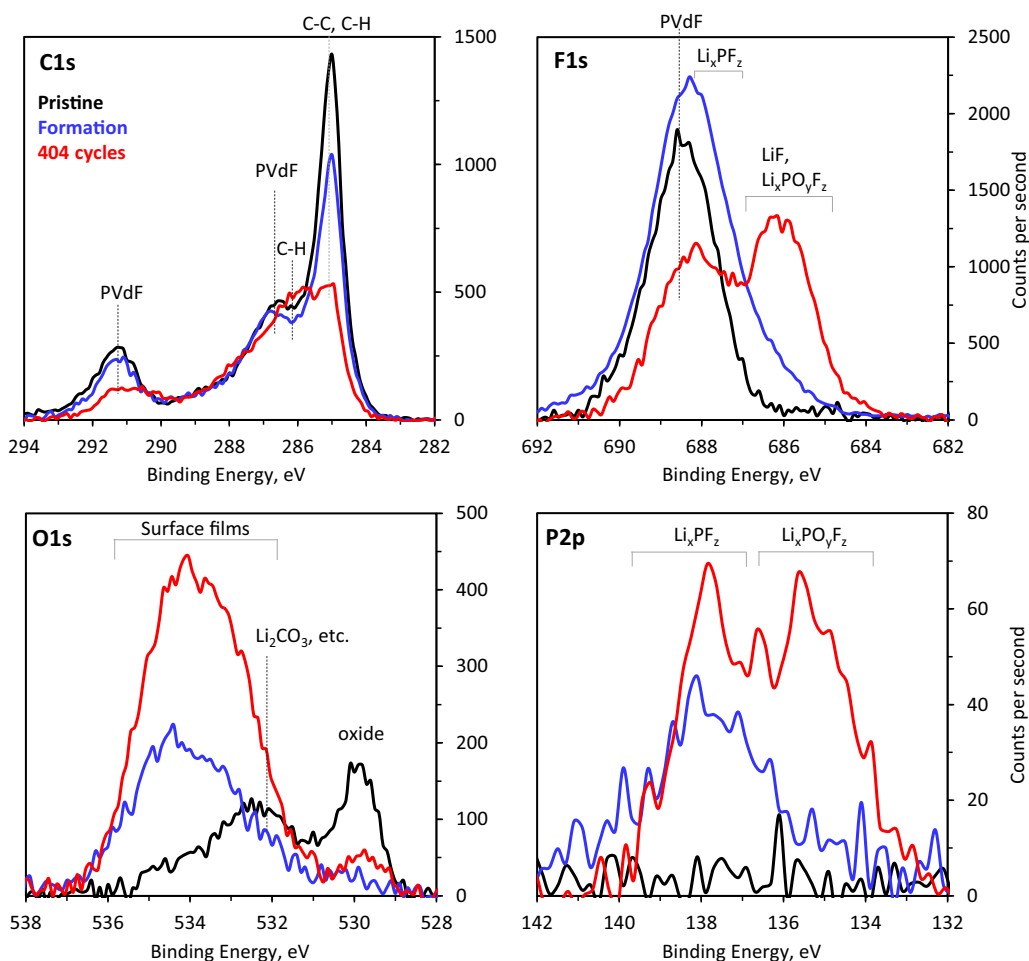
Figure 12. XPS spectra (C1s, O1s, F1s, P2p) from positive electrodes harvested from cells after formation cycling (blue) and after 404 cycles (red). Spectra from pristine electrodes (black) are included for comparison. Note that the Binding energy (X-axis) and Intensity scale (Y-axis) are different for each plot.

Summary and Concluding Remarks

As described above the loss of cyclable lithium-ions within the full cell results from undesired side reactions in the negative electrode SEI. In the initial cycles this SEI (formed from electrolyte break-down products) is essential to block the access of solvent molecules from intercalating into the graphite while allowing the passage of Li^+ ions. This SEI is relatively thin (as indicated by the SIMS data) and comprises mainly of organic species (as indicated by the XPS data). On continued cycling, however, the SEI layer thickens (Fig. 10) and becomes more inorganic as seen from the increase in lithium, fluorine, phosphorous and oxygen concentrations (Fig. 11). The SEI thickening results from continual electrolyte reduction on fresh surfaces at graphite particle edges, exposed as a result of small-scale fractures during the Li^+ ion intercalation-deintercalation process.[5] The progress toward an inorganic SEI probably results from the partial dissolution of organic components into the electrolyte during the charge-discharge cycling.

In the research literature the capacity loss of lithium-ion cells is often reported to increase with the square root of time.[38,54] Ploehn et al. presented a one-dimensional solvent diffusion model to explain this dependence and concluded that the SEI thickness also grows in proportion to the square root of time.[55] Smith et al. also reached the same conclusion from a high precision coulometry study of Li/graphite coin cells.[38] Pinson and Bazant also noted the square root of time dependence for the formation of a stable SEI layer well adhered to the electrode.[56] For systems with "unstable SEI", however, they noted other dependencies including a linear SEI growth with time.

In our present experiments the loss of cyclable lithium-ions shows a linear dependence with time. It is important to note here that in most articles that report full cell cycling data the upper cutoff voltage (UCV) is typically limited to less than 4.2 V. In our experiments, the full cell UCV is 4.4 V, and the upper potential for the positive electrodes is ∼4.5 V vs. Li/Li^+, which is known to increase the dissolution of transition metal elements from the positive electrode.[50] This process is further accelerated by the shifts in electrode potential windows, which causes the positive electrode to cycle at higher states-of-charge as aging progresses. The diffusion of transition metal ions, such as Mn^{+2}, through the electrolyte and deposition at the graphite negative electrode (see SIMS data) is known to correlate with higher cell capacity fade.[57–59] The increased Li-trapping side reactions, because of higher transition metal ion contents in the SEI layer, may explain the linear rather than the square root of time dependence. We have shown previously that the location and oxidation state of the Mn are critical to the extent of capacity fade.[50] Manganese presence in the inner SEI layer is a problem because the Mn^{+2} ions are reduced further to an unidentified species. This reduced Mn species reacts with the solvent that oxidizes it back to Mn^{+2}. The electrolyte breakdown products contain carboxylate groups such as ethylene dicarbonate, which associate with Li^+ ions, causing their retention in the SEI, and reducing the cyclable Li^+ ion content in the cell.

In addition to capacity fade our cells show significant impedance growth. This impedance reduces both cell charge and discharge capacities by shortening the time required to reach the upper and lower cutoff voltages at the cycling current. The impedance increases arise mainly at the positive electrode though some increase is also evident

at the negative electrode. As the bulk graphite particles are not damaged on cycling[5] the latter impedance rise probably results from the increasing inorganic components in the SEI layer. Because the SEI grows significantly (as seen from the SIMS and XPS data) it is surprising that the impedance rise at the electrode is relatively small. The relatively rapid diffusion of Li$^+$ through the SEI is apparently a consequence of the arrangement of the EC-derived polymer chains that are "zipped" by Li$^+$ ions that have a tetrahedral coordination and are shared by two carbonate groups;[60] Li$^+$ conduction can occur through an ion-exchange mechanism, with the incoming Li$^+$ ion releasing bound Li$^+$ ions.[61] In the inorganic layer diffusion of Li$^+$ ions likely occurs by a repetitive knock-off mechanism than by direct hopping through the empty spaces between the lattice sites.[62] Both knock-off (in the inorganics) and zipping (in the organics) mechanisms are facilitated by the abundance (and increasing content) of Li$^+$ ions in the SEI layer.

The impedance increases at the positive electrode include contributions from the surface films that contain inorganic compounds, such as LiF and Li$_x$PO$_y$F$_z$, which are electrolyte breakdown products (see XPS data). However, these surface films are relatively thin and, furthermore, cannot explain the voltage dependence of the impedance increase – see Figure 7, which shows higher impedance growth at the higher cell voltages. Therefore, we continue to investigate the causal reasons for the positive electrode impedance rise. Initial results indicate that structural changes at the oxide particle surface, similar to those described for LiNi$_{0.8}$Co$_{0.2}$O$_2$ and other oxides, are an important contributor.[30,63–65] In addition, the increasing separation of primary particles within the secondary particles because of anisotropic expansion and contraction during delithiation and lithiation processes play a major role in impedance growth during extended cell cycling.[66,67] Detailed results from these ongoing studies will be presented in future articles.

References

1. M. M. Thackeray, C. Wolverton, and E. D. Isaacs, *Energy & Environmental Science*, **5**, 7854 (2012).

2. M. M. Thackeray, S. H. Kang, C. S. Johnson, J. T. Vaughey, R. Benedek, and S. A. Hackney, *Journal of Materials Chemistry*, **17**, 3112 (2007).
3. B. Qiu, M. Zhang, L. Wu, J. Wang, Y. Xia, D. Qian, H. Liu, S. Hy, Y. Chen, K. An, Y. Zhu, Z. Liu, and Y. S. Meng, *Nat Commun*, **7**, (2016).
4. M. Bettge, Y. Li, B. Sankaran, N. D. Rago, T. Spila, R. T. Haasch, I. Petrov, and D. P. Abraham, *Journal of Power Sources*, **233**, 346 (2013).
5. Y. Li, M. Bettge, B. Polzin, Y. Zhu, M. Balasubramanian, and D. P. Abraham, *Journal of The Electrochemical Society*, **160**, A3006 (2013).
6. Y. Zhu, Y. Li, M. Bettge, and D. P. Abraham, *Electrochim. Acta*, **110**, 191 (2013).
7. T. Ohzuku, M. Nagayama, K. Tsuji, and K. Ariyoshi, *Journal of Materials Chemistry*, **21**, 10179 (2011).
8. S. Hy, H. Liu, M. Zhang, D. Qian, B.-J. Hwang, and Y. S. Meng, *Energy & Environmental Science*, **9**, 1931 (2016).
9. J. Zheng, M. Gu, J. Xiao, P. Zuo, C. Wang, and J.-G. Zhang, *Nano Letters*, **13**, 3824 (2013).
10. J. Hong, H. Gwon, S.-K. Jung, K. Ku, and K. Kang, *Journal of The Electrochemical Society*, **162**, A2447 (2015).
11. M. Bettge, Y. Li, K. Gallagher, Y. Zhu, Q. Wu, W. Lu, I. Bloom, and D. P. Abraham, *Journal of The Electrochemical Society*, **160**, A2046 (2013).
12. K. G. Gallagher, J. R. Croy, M. Balasubramanian, M. Bettge, D. P. Abraham, A. K. Burrell, and M. M. Thackeray, *Electrochemistry Communications*, **33**, 96 (2013).
13. J. R. Croy, M. Balasubramanian, K. G. Gallagher, and A. K. Burrell, *Accounts of Chemical Research*, **48**, 2813 (2015).
14. D. Mohanty, A. Huq, E. A. Payzant, A. S. Sefat, J. Li, D. P. Abraham, D. L. Wood, and C. Daniel, *Chemistry of Materials*, **25**, 4064 (2013).
15. D. Mohanty, A. S. Sefat, J. Li, R. A. Meisner, A. J. Rondinone, E. A. Payzant, D. P. Abraham, D. L. Wood Iii, and C. Daniel, *Physical Chemistry Chemical Physics*, **15**, 19496 (2013).
16. A. Boulineau, L. Simonin, J.-F. Colin, E. Canévet, L. Daniel, and S. Patoux, *Chemistry of Materials*, **24**, 3558 (2012).
17. Y. Li, M. Bettge, J. Bareño, S. E. Trask, and D. P. Abraham, *Journal of The Electrochemical Society*, **162**, A7049 (2015).
18. Y. Li, J. Bareño, M. Bettge, and D. P. Abraham, *Journal of The Electrochemical Society*, **162**, A155 (2015).
19. M. Sathiya, A. M. Abakumov, D. Foix, G. Rousse, K. Ramesha, M. Saubanère, M. L. Doublet, H. Vezin, C. P. Laisa, A. S. Prakash, D. Gonbeau, G. VanTendeloo, and J. M. Tarascon, *Nat Mater*, **14**, 230 (2015).
20. P. Bernard, H. Martinez, C. Tessier, E. Garitte, S. Franger, and R. Dedryvere, *Journal of The Electrochemical Society*, **162**, A7096 (2015).
21. W. Qiu, J. Xia, L. Chen, and J. R. Dahn, *Journal of Power Sources*, **318**, 228 (2016).
22. J. Xia, L. Ma, and J. R. Dahn, *Journal of Power Sources*, **287**, 377 (2015).
23. I. Buchberger, S. Seidlmayer, A. Pokharel, M. Piana, J. Hattendorff, P. Kudejova, R. Gilles, and H. A. Gasteiger, *Journal of The Electrochemical Society*, **162**, A2737 (2015).
24. S. Li, X. Fu, J. Zhou, Y. Han, P. Qi, X. Gao, X. Feng, and B. Wang, *Journal of Materials Chemistry A*, **4**, 5823 (2016).
25. R. D. Deshpande, P. Ridgway, Y. Fu, W. Zhang, J. Cai, and V. Battaglia, *Journal of The Electrochemical Society*, **162**, A330 (2015).
26. X. Zheng, X. Li, Z. Wang, H. Guo, Z. Huang, G. Yan, and D. Wang, *Electrochimica Acta*, **191**, 832 (2016).
27. S.-M. Bak, E. Hu, Y. Zhou, X. Yu, S. D. Senanayake, S.-J. Cho, K.-B. Kim, K. Y. Chung, X.-Q. Yang, and K.-W. Nam, *ACS Applied Materials & Interfaces*, **6**, 22594 (2014).
28. R. Amin and Y.-M. Chiang, *Journal of The Electrochemical Society*, **163**, A1512 (2016).
29. M. Dixit, M. Kosa, O. S. Lavi, B. Markovsky, D. Aurbach, and D. T. Major, *Physical Chemistry Chemical Physics*, **18**, 6799 (2016).
30. S.-K. Jung, H. Gwon, J. Hong, K.-Y. Park, D.-H. Seo, H. Kim, J. Hyun, W. Yang, and K. Kang, *Advanced Energy Materials*, **4**, (2014).
31. D. Aurbach, O. Srur-Lavi, C. Ghanty, M. Dixit, O. Haik, M. Talianker, Y. Grinblat, N. Leifer, R. Lavi, D. T. Major, G. Goobes, E. Zinigrad, E. M. Erickson, M. Kosa, B. Markovsky, J. Lampert, A. Volkov, J.-Y. Shin, and A. Garsuch, *Journal of The Electrochemical Society*, **162**, A1014 (2015).
32. Y.-M. Lee, K.-M. Nam, E.-H. Hwang, Y.-G. Kwon, D.-H. Kang, S.-S. Kim, and S.-W. Song, *The Journal of Physical Chemistry C*, **118**, 10631 (2014).
33. W. Hua, J. Zhang, Z. Zheng, W. Liu, X. Peng, X.-D. Guo, B. Zhong, Y.-J. Wang, and X. Wang, *Dalton Transactions*, **43**, 14824 (2014).
34. D. P. Abraham, J. L. Knuth, D. W. Dees, I. Bloom, and J. P. Christophersen, *Journal of Power Sources*, **170**, 465 (2007).
35. D. P. Abraham, T. Spila, M. M. Furczon, and E. Sammann, *Electrochem. Solid-State Lett.*, **11**, A226 (2008).
36. I. Bloom, A. N. Jansen, D. P. Abraham, J. Knuth, S. A. Jones, V. S. Battaglia, and G. L. Henriksen, *Journal of Power Sources*, **139**, 295 (2005).
37. I. Bloom, J. P. Christophersen, D. P. Abraham, and K. L. Gering, *Journal of Power Sources*, **157**, 537 (2006).
38. A. J. Smith, J. C. Burns, X. Zhao, D. Xiong, and J. R. Dahn, *Journal of The Electrochemical Society*, **158**, A447 (2011).
39. D. P. Abraham, D. W. Dees, J. Christophersen, C. Ho, and A. N. Jansen, *Int. J. Energy Res.*, **34**, 190 (2010).
40. D. P. Abraham, S. D. Poppen, A. N. Jansen, J. Liu, and D. W. Dees, *Electrochim. Acta*, **49**, 4763 (2004).
41. D. Dees, E. Gunen, D. Abraham, A. Jansen, and J. Prakash, *Journal of the Electrochemical Society*, **155**, A603 (2008).
42. D. Dees, E. Gunen, D. Abraham, A. Jansen, and J. Prakash, *Journal of the Electrochemical Society*, **152**, A1409 (2005).

43. D. P. Abraham, J. R. Heaton, S. H. Kang, D. W. Dees, and A. N. Jansen, *Journal of the Electrochemical Society*, **155**, A41 (2008).
44. D. P. Abraham, S. Kawauchi, and D. W. Dees, *Electrochimica Acta*, **53**, 2121 (2008).
45. D. W. Dees, D. P. Abraham, W. Lu, K. G. Gallagher, M. Bettge, and A. N. Jansen, *Journal of The Electrochemical Society*, **162**, A559 (2015).
46. H. Liu, J. M. Foster, A. Gully, S. Krachkovskiy, M. Jiang, Y. Wu, X. Yang, B. Protas, G. R. Goward, and G. A. Botton, *Journal of Power Sources*, **306**, 300 (2016).
47. S. E. Trask, Y. Li, J. J. Kubal, M. Bettge, B. J. Polzin, Y. Zhu, A. N. Jansen, and D. P. Abraham, *J. Power Sources*, **259**, 233 (2014).
48. R. Kostecki, L. Norin, X. Song, and F. McLarnon, *Journal of The Electrochemical Society*, **151**, A522 (2004).
49. Y. Zhu, Y. Li, M. Bettge, and D. P. Abraham, *Journal of The Electrochemical Society*, **159**, A2109 (2012).
50. I. A. Shkrob, A. J. Kropf, T. W. Marin, Y. Li, O. G. Poluektov, J. Niklas, and D. P. Abraham, *The Journal of Physical Chemistry C*, **118**, 24335 (2014).
51. A. Xiao, L. Yang, B. L. Lucht, S.-H. Kang, and D. P. Abraham, *Journal of The Electrochemical Society*, **156**, A318 (2009).
52. M. Herstedt, D. P. Abraham, J. B. Kerr, and K. Edstrom, *Electrochimica Acta*, **49**, 5097 (2004).
53. A. M. Andersson, D. P. Abraham, R. Haasch, S. MacLaren, J. Liu, and K. Amine, *Journal of the Electrochemical Society*, **149**, A1358 (2002).
54. M. Broussely, S. Herreyre, P. Biensan, P. Kasztejna, K. Nechev, and R. J. Staniewicz, *Journal of Power Sources*, **97–98**, 13 (2001).
55. H. J. Ploehn, P. Ramadass, and R. E. White, *Journal of The Electrochemical Society*, **151**, A456 (2004).
56. M. B. Pinson and M. Z. Bazant, *Journal of The Electrochemical Society*, **160**, A243 (2013).
57. N. P. W. Pieczonka, Z. Liu, P. Lu, K. L. Olson, J. Moote, B. R. Powell, and J.-H. Kim, *The Journal of Physical Chemistry C*, **117**, 15947 (2013).
58. A. Jarry, S. Gottis, Y.-S. Yu, J. Roque-Rosell, C. Kim, J. Cabana, J. Kerr, and R. Kostecki, *Journal of the American Chemical Society*, **137**, 3533 (2015).
59. H. Tsunekawa, S. Tanimoto, Satoshi, R. Marubayashi, M. Fujita, K. Kifune, and M. Sano, *Journal of The Electrochemical Society*, **149**, A1326 (2002).
60. I. A. Shkrob, Y. Zhu, T. Marin, and D. P. Abraham, *J. Phys. Chem. C*, **117**, 19270 (2013).
61. O. Borodin, G. V. Zhuang, P. N. Ross, and K. Xu, *J. Phys. Chem. C*, **117**, 7433 (2013).
62. S. Shi, P. Lu, Z. Liu, Y. Qi, L. G. Hector, H. Li, and S. J. Harris, *J. Am. Chem. Soc.*, **134**, 15476 (2012).
63. H. Kuriyama, H. Saruwatari, H. Satake, A. Shima, F. Uesugi, H. Tanaka, and T. Ushirogouchi, *Journal of Power Sources*, **275**, 99 (2015).
64. D. P. Abraham, R. D. Twesten, M. Balasubramanian, I. Petrov, J. McBreen, and K. Amine, *Electrochem. Commun.*, **4**, 620 (2002).
65. D. P. Abraham, R. D. Twesten, M. Balasubramanian, J. Kropf, D. Fischer, J. McBreen, I. Petrov, and K. Amine, *J. Electrochem. Soc.*, **150**, A1450 (2003).
66. D. J. Miller, C. Proff, J. G. Wen, D. P. Abraham, and J. Bareño, *Advanced Energy Materials*, **3**, 1098 (2013).
67. W. H. Woodford, W. C. Carter, and Y.-M. Chiang, *Energy & Environmental Science*, **5**, 8014 (2012).